

PAPER • OPEN ACCESS

A new approach for alkali incorporation in $\text{Cu}_2\text{ZnSnS}_4$ solar cells

To cite this article: M Valdés *et al* 2022 *J. Phys. Energy* **4** 044008

View the [article online](#) for updates and enhancements.

You may also like

- [Study on the Harm of Saline Alkali Land and Its Improvement Technology in China](#)
Baoqiang Zhang and Na Wang
- [Solution- Processed Alkali Metals-Doped Amorphous Zinc Tin Oxide Thin-Film Transistors and Analysis of Alkali Metal Doping Mechanism through the UV-Visible Spectroscopic](#)
Keon-Hee Lim, Eungkyu Lee, Kyongjun Kim *et al.*
- [Lifecycle assessment of alkali activated cement concrete](#)
Angitha K Viswanath and K B Anand



PAPER

A new approach for alkali incorporation in $\text{Cu}_2\text{ZnSnS}_4$ solar cells

OPEN ACCESS

M Valdés^{1,*}, A Hernández², Y Sánchez², R Fonoll², M Placidi^{2,3}, V Izquierdo²,
A Cabas-Vidani⁴, M Valentini⁵, A Mittiga⁵, P Pistor⁶, C Malerba⁵ and E Saucedo³

RECEIVED
14 July 2022

REVISED
20 September 2022

ACCEPTED FOR PUBLICATION
30 September 2022

PUBLISHED
14 October 2022

Original content from
this work may be used
under the terms of the
[Creative Commons
Attribution 4.0 licence](#).

Any further distribution
of this work must
maintain attribution to
the author(s) and the title
of the work, journal
citation and DOI.



¹ Instituto de Investigaciones en Ciencia y Tecnología de Materiales (INTEMA), CONICET-UNMdP, Av. Cristóbal Colón 10850, Mar del Plata B7606WV, Argentina

² Catalonia Institute for Energy Research (IREC), 08930 Sant Adrià del Besòs, Barcelona, Spain

³ Electronic Engineering Department, Polytechnic University of Catalonia (UPC), Campus Besòs, Av. d'Eduard Maristany, 16, Barcelona 08930, Spain

⁴ Laboratory for Thin Films and Photovoltaics, Empa-Swiss Federal Laboratories for Materials Science and Technology, Ueberlandstrasse 129, Duebendorf 8600, Switzerland

⁵ ENEA, Casaccia Research Center, via Anguillarese 301, Roma 00123, Italy

⁶ University Pablo de Olavide Physical Chemistry Section, Ctra. de Utrera, 1, Sevilla 41013, España

* Author to whom any correspondence should be addressed.

E-mail: mvaldes@fi.mdp.edu.ar

Keywords: kesterite, CZTS, alkali doping, CBD, PDA, thin film photovoltaics

Supplementary material for this article is available [online](#)

Abstract

The addition of alkali elements has become mandatory for boosting solar cell performance in chalcogenide thin films based on kesterites ($\text{Cu}_2\text{ZnSnS}_4$, CZTS). A novel doping process is presented here, that consists in the incorporation of sodium or lithium during the deposition of the CdS buffer layer, followed by a post-deposition annealing (PDA). As the doping route leads to more efficient devices in comparison with the undoped reference sample, the influence of PDA temperature was also investigated. Compositional profiling techniques, time-of-flight secondary ion mass spectrometry (TOF-SIMS) and glow discharge optical mission spectroscopy (GDOES), revealed a dependence of the alkaline distribution in kesterites with the PDA temperature. Although the doping process is effective in that it increases the alkaline concentration compared to the undoped sample, the compositional profiles indicate that a significant proportion of Li and Na remains 'trapped' within the CdS layer. In the 200 °C–300 °C range the alkali profiles registered the higher concentration inside the kesterite. Despite this, an additional alkali accumulation close to the molybdenum/fluorine doped tin oxide substrate was found for all the samples, which is frequently related to alkali segregation at interfaces. The addition of both, lithium and sodium, improves the photovoltaic response compared to the undoped reference device. This is mainly explained by a substantial improvement in the open-circuit potential (V_{oc}) of the cells, with best devices achieving efficiencies of 4.5% and 3% for lithium and sodium, respectively. Scanning-electron microscopy images depicted a 'bilayer structure' with larger grains at the top and small grains at the bottom in all samples. Moreover, the calculated bandgap energies of the CZTS films account for changes in the crystallographic order-disorder of the kesterites, more related to the PDA treatment rather than alkali incorporation. Even if further optimization of the absorber synthesis and doping process will be required, this investigation allowed the evaluation of a novel strategy for alkali incorporation in kesterite based solar cells.

1. Introduction

In search of new affordable and ecofriendly technologies, the photovoltaic (PV) research community has been strongly committed into developing research lines for non-toxic, non-critical, earth-abundant materials. Kesterite based materials composed of $\text{Cu}_2\text{ZnSnS}_4$ (CZTS), $\text{Cu}_2\text{ZnSnSe}_4$ (CZTSe) or their corresponding solid solution $\text{Cu}_2\text{ZnSn}(\text{S},\text{Se})_4$ (CZTSSe) fulfill all these pre-requisites [1, 2]. In addition,

kesterites are very suitable for PV as they show an absorption coefficient $>10^4 \text{ cm}^{-1}$, an intrinsic p-type conductivity, and a direct band gap (BG) ranging from 1.0–1.5 eV depending on the S/(S + Se) content [3, 4].

Kesterite solar cell performance is still hindered by the high V_{oc} -deficit which leads to a low record efficiency (12.6%) compared with Cu(In,Ga)(S,Se)₂ (CIGS) solar cells (23.35%) [5]. In order to overcome these limitations alkali doping of kesterite films has been employed [6] proving its beneficial effects by reducing voltage deficit [7], increasing net hole carrier concentrations [8], passivating grain boundaries [9] and increasing grain size [10]. A recent review describes the main methods and achievements obtained by alkali doping [6]. Na can be introduced by using a layer of molybdenum doped with sodium (Mo:Na), by using evaporated NaF layers [11], or by addition of concentrated NaCl in solution processed kesterites [12, 13]. For lithium, the routes can be quite different because Li has also the ability to alloy with kesterite and is usually included during the precursor synthesis [6].

The use of post-deposition annealing (PDA) treatments has been extended to various thin-film photovoltaic technologies. In CIGS technology, the benefits of treatments in air at low temperatures (100 °C–200 °C) have been widely reported [14, 15]. In the case of kesterite, the PDA treatments have been carried out to modify the cation ordering state of the absorber [16, 17], to promote the incorporation of dopants or alloying elements [6, 18], or to thermally activate the diffusion of some specific element already present in the device, such as the Cd migration across the junction [19, 20] or alkali diffusion from the substrate to the kesterite [9, 21].

In this work, we developed a novel strategy for alkali incorporation in CZTS thin film deposited on fluorine doped tin oxide (FTO)/Mo substrates. This approach employs a soft chemistry route, where alkaline elements (Li and Na) are incorporated into the chemical bath used for the deposition (CBD) of the CdS buffer layer. Later, a low temperature PDA of the CZTS/CdS heterojunction completes the doping process with the aim of improving the alkali distribution inside the CZTS absorber. Mo-covered FTO substrates were used for these studies. FTO is known to act as a barrier against alkali diffusion and it is here used to avoid uncontrolled diffusion of sodium from the glass, improving the control of the doping process whereas Mo is the standard contact used par excellence in PV chalcogenide technology. However, being Mo an opaque material, it has certain limitations and, since the initial work of Nakada *et al* [22], there has been a strong investigation to adapt high transparency substrates to chalcopyrite and kesterite technology aiming to expand its application to other types of devices such as: tandem solar cells [23], bi-facial solar cells [24–26] or semi-transparent devices [27, 28]. In this perspective, very thin (20 nm) Mo films were deposited onto FTO aiming to obtain, during the sulfurization process, a total conversion of Mo into a semitransparent MoS₂ layer acting as a selective contact to the FTO. The electrical contact of such FTO/MoS₂ back contact with CZTS is supposed to be similar to that obtained with standard (thicker) Mo films, since an interfacial MoS₂ layer typically forms between Mo and CZTS.

2. Materials and methods

2.1. Precursor and absorber deposition

The experimental procedure is graphically described in figure 1. FTO glasses (800 nm, 10 Ω/□) were employed as substrates in order to improve the control of the alkali doping of CZTS by blocking uncontrolled Na diffusion from the glass. First, a Mo nanolayer (≈20 nm) was deposited by direct current (DC) sputtering on the substrate, to promote its total conversion in MoS₂ during the reactive sulfurization step. The thickness of the Mo nanolayer was chosen on the basis of a previous publication of the group [24].

Then Cu–Zn–Sn–S quaternary precursors were obtained by combining direct current (DC) and radio frequency (RF) co-sputtering of three circular targets (4 inches' diameter) of Cu, SnS, and ZnS (Cu: DC, 28 W; SnS: RF, 80 W; ZnS: RF, 160 W) in an Oerlikon-UNIVEX 450B sputtering system. The working pressure was 5×10^{-3} mbar, with an Ar flux of 50 sccm, and no intentional heating of the substrates during deposition. $2.5 \times 2.5 \text{ cm}^2$ sputtered precursors were sulfurized in a S + Sn containing atmosphere (100 mg of S and 5 mg of Sn (Alfa-Aesar powder, 100 mesh, 99.995%)), using a semi-closed graphite box (69 cm³ in volume) in a conventional tubular furnace. The sulfurization was performed in a two-step process, the first one at 200 °C (heating ramp of 20 °C min⁻¹) during 15 min at 1.5 mbar Ar pressure, followed by a second step at 550 °C (heating ramp also of 20 °C min⁻¹) during 30 min at a pressure of nearly 1 bar, with a natural cooling down to room temperature.

After sulfurization and conversion of the sputtered precursor in CZTS, samples were etched in (NH₄)₂S in order to remove possible secondary Sn(S) phases and to promote surface passivation [29].

Two different sets of samples, doped with Li or Na, were obtained by means of a 'CdS-doping step'. In our standard CBD process for CdS deposition we use cadmium nitrate as a source of Cd²⁺. So, CBD conditions were (Cd(NO₃)₂) = 0.12 mol l⁻¹, (SC(NH₂)₂) = 0.3 mol l⁻¹, pH = 9.5, and the $T = 70 \text{ °C}$. In this particular CBD process, concentrated (2 mol l⁻¹) Li₃C₆H₅O₇ or Na₃C₆H₅O₇ salts were introduced inside the

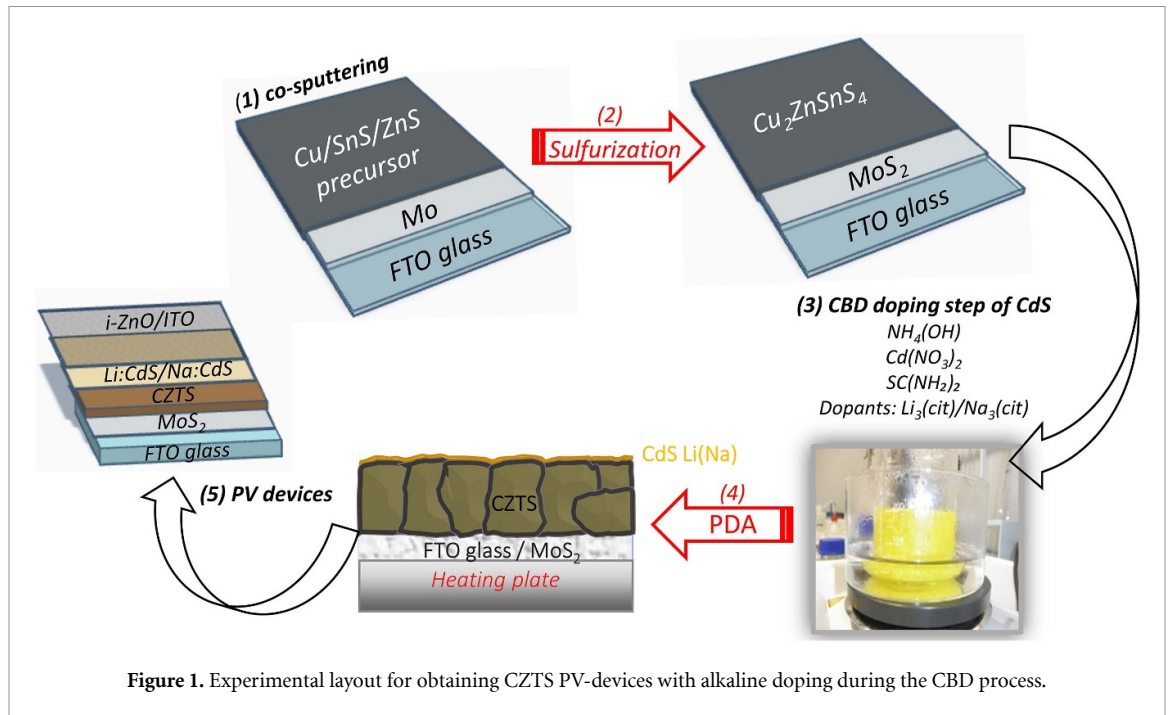


Figure 1. Experimental layout for obtaining CZTS PV-devices with alkaline doping during the CBD process.

Table 1. Nomenclature and experimental details of the samples under study.

N°	1st step	2nd step	3th step	PDA
References (PDA_300)	Sulfurization	CdS (undoped)	PDA	300 °C_10 min
Na/Li_200	Sulfurization	Na/Li:CdS-doping	PDA	200 °C_10 min
Na/Li_250	Sulfurization	Na/Li:CdS-doping	PDA	250 °C_10 min
Na/Li_300	Sulfurization	Na/Li:CdS-doping	PDA	300 °C_10 min
Na/Li_350	Sulfurization	Na/Li:CdS-doping	PDA	350 °C_10 min
Na/Li_400	Sulfurization	Na/Li:CdS-doping	PDA	400 °C_10 min

chemical bath used for CdS deposition, for Li and Na doping respectively. In all cases the CdS deposition time was kept at 40 min. More details about the CBD process can be found in [30]. To complete the doping process, the processed CZTS/CdS junctions were exposed to a PDA treatment in a hot plate inside a fume hood with controlled humidity (<20%) and temperature (25 °C) values. The PDA treatment was used in the range from 200 °C to 400 °C to evaluate how the temperature affects the alkali distribution and optoelectronic parameters of PV devices. Table 1 summarize the nomenclature and experimental features of each sample. A reference sample was included where no alkalis were intentionally introduced during the CdS deposition. With the intention to isolate the effect of alkali doping during the CBD deposition, and for the sake of comparison, the PDA treatment was also performed in the reference sample at 300 °C. For more clarity, this sample is labeled 'Ref (PDA_300)'.

2.2. Material characterization

Cross-section images were obtained in selected samples using scanning-electron microscopy (SEM, Zeiss LEO 35). A depth-profiling analysis of the Na doped samples was performed by GDOES measurements using a HORIBA Jobin Yvon GD Profiler spectrometer, equipped with an anode diameter of 4 mm and 19 element channels. Depth profile measurements of Li doped samples were performed with a TOF-SIMS system from ION-TOF using O^{+2} primary ions with 2 keV of ion energy, a current of about 300 nA, and a raster size of $300 \times 300 \mu m^2$. An area of $100 \times 100 \mu m^2$ in the case of depth profiles was analyzed using Bi^+ ions with 25 keV of ion energy.

2.3. Device preparation

After PDA treatments, solar cells devices were completed by DC-pulsed sputtering deposition (Alliance CT100) of i-ZnO (50 nm) and ITO (200 nm) as a transparent conductive window layer. For optoelectronic characterization, $3 \times 3 \text{ mm}^2$ cells were mechanically scribed using a manual microdiamond scriber (MR200 OEG). Neither antireflective coating nor metallic grids were deposited on the solar cells.

2.4. Device characterization

Solar cells devices were characterized by current density-voltage (J - V) measurements under simulated illumination conditions using a calibrated Sun 3000 Class AAA solar simulator (1-Sun AM1.5, Abet Technologies). Full external quantum efficiency (EQE) and internal quantum efficiency (IQE) characterization were obtained using a Bentham PVE300. Statistical results arise from measurements made in number of cells that varies between 8 and 12 depending on each sample.

3. Results

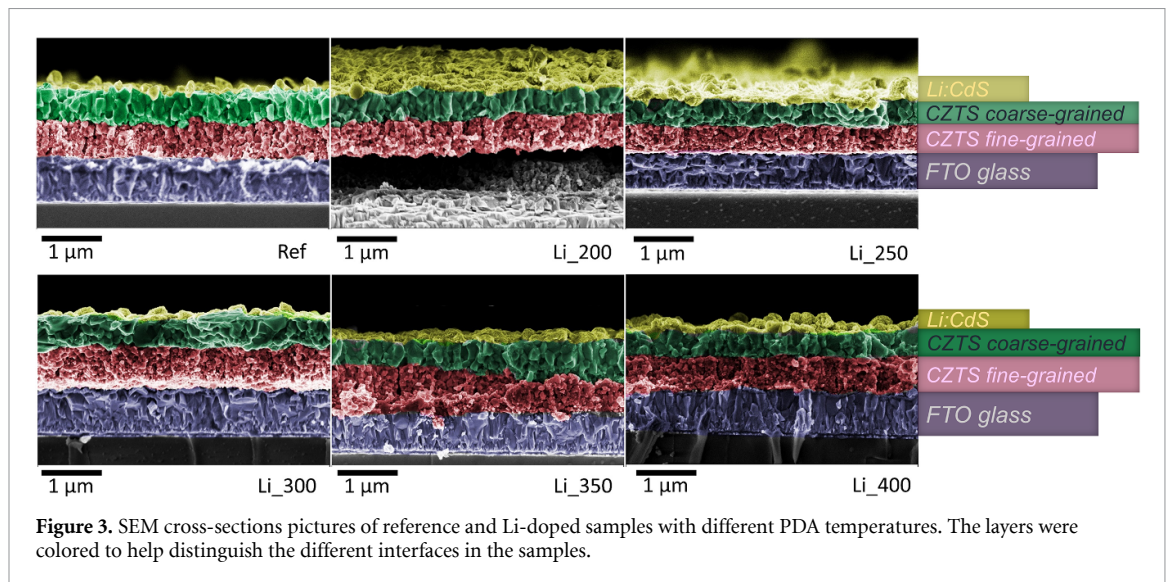
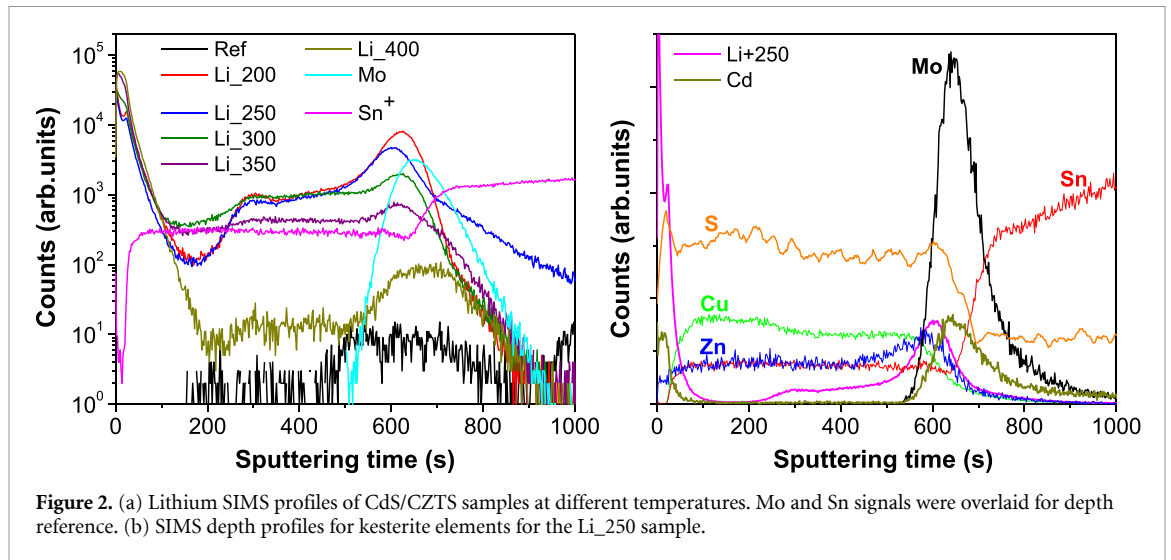
For a better analysis of the effect of each alkaline, we will present separately the results of the samples doped with lithium and then with sodium.

3.1. Li doped samples

The distribution of lithium within the samples has been studied through TOF-SIMS measurements. Figure 2(a) shows Li depth profiles for Li-doped samples (CdS/CZTS junctions) with PDA at different temperatures. Log-scale was chosen to get a clearer comparison among all the Li profiles. Leaving aside the reference sample where there is no lithium signal (as expected), a diffusion profile of lithium can be observed in all the doped films. In more detail lithium profiles show a high concentration at the top surface, that could be related to incorporation of Li in the CdS layer (CdS doping) [31, 32], or to Li (or Li-compounds) segregation at the top interfaces (sample surface and CdS/CZTS interface). Besides, Li is unevenly distributed inside the kesterite, with lower concentration in the upper region of the CZTS (sputtering time 20–300 s) and higher accumulation in the rear region (sputtering time 300–500 s) and at the back contact interface (peak around 600 s).

This behavior could be explained looking at the cross-sectional SEM pictures depicted in figure 3. Indeed, it is known from the literature that, compared to heavier alkali elements which tend to segregate at grain boundaries, lithium can be incorporated at much higher quantities by alloying with kesterite phase forming a solid solution [6, 33–35]. However, for concentration higher than its maximum solubility, segregations of not-alloyed Li or Li compounds can be expected at grain boundaries or interfaces. This hypothesis can explain the inhomogeneous Li distribution observed in our sample, since the rear region of CZTS is characterized by small grains, corresponding to a higher grain boundaries density (and therefore higher Li content) compared to the top region, where larger grains grew after sulfurization. Then the second ‘hump’ (peak at sputtering time around 600 s) suggest Li segregation also at the back interface. This segregation at the CZTS/MoS₂ interface is more noticeable at low PDA temperatures (200 °C–250 °C). Oddly, at higher temperatures the profiles become flatter (300 °C–350 °C), or the lithium concentration drops abruptly (400 °C). For this latter case, the profile is striking, because at the surface the concentration is high but inside the kesterite is noticeably lower. Further studies are needed to elucidate this behavior. We do not discard an enhanced possible diffusion of Li inside Mo/FTO layer at higher temperature. Figure 2(b) shows SIMS depth profiles of relevant elements in the Li:CdS/CZTS heterojunction annealed at 250 °C. The complete set of SIMS profiles for all the samples is presented in figure S1 in the supplementary information file (SI). For the sake of clarity, signal intensities were arbitrarily rescaled according to the C₂ZnSnS₄ formula ratio. Flat profiles of CZTS elements (Cu, Zn, Sn and S) can be observed. A slightly increment in the Zn profile near the Mo interface is seen that can be related to a frequently reported zinc segregation normally detected as ZnS [36]. The Cd signal is more likely to be a matrix effect with the Mo signals rather than a diffusion behavior of this element [24].

Cross-section SEM pictures are presented in figure 3. To highlight the different materials and morphologies, the pictures were intentionally colored. All the samples present a similar morphology, because, leaving aside the PDA temperature, they were processed in an analogous way regarding precursor sputtering, sulfurization and doping stages. In fact, characterization by x-ray diffraction (XRD) and Raman spectroscopy also revealed a high degree of similarity in terms of composition and crystalline phases present in the samples (see figures S4–S6, SI file). CZTS films present a ‘double layer morphology’ with larger grains on top and smaller at the bottom close to the FTO/Mo substrate. This type of bi-layer structure has been previously reported, in kesterite grown on transparent or semi-transparent substrates [24, 37]; and even in standard Mo glass substrates [38–41]. The reasons that explain the formation of this double morphology remain unclear and have been associated with different experimental results. In a recent work, Martinho *et al* have reviewed the existing research on double-layered kesterites trying to shed some light about this phenomenon [42]. As common factors, for physical and solution deposition methods, the presence of metallic Cu and/or a chalcogen deficiency in the precursor matrix have been proposed by the authors as main reasons determining the double-layer occurrence. Although the samples have higher lithium content compared to the reference, which indicates that the doping process is effective, high-efficiency devices usually show flat alkaline profiles



within the kesterite absorber [33]. Figure 4 shows statistic optoelectronic parameters for Li doped and reference samples. The doping process improves the V_{oc} of all the cells compared to the reference device with no doping. In contrast, the fill factor (FF) of the devices only improves over the reference at intermediate PDA temperatures (250 °C–300 °C). The FF variations can partly explain the low value of the short circuit current (J_{SC}) of the Li₂₀₀ sample and the high J_{SC} value of the Li₃₀₀ sample. The product of these three parameters finally determines the conversion efficiency of the devices: the highest values are obtained with PDA temperatures of 300 °C, where the best device achieves an efficiency of 4.5%.

3.2. Na doped samples

Figure 5 presents a GDOES analysis performed to study the Na distribution inside the processed samples. Figure 5(a) shows Na distribution for doped CdS/CZTS samples with PDA at different temperatures. First, a significant difference is observed in terms of the sodium content of the doped samples compared to the reference sample (no doping). This proves that the sodium from the CdS buffer deposition has indeed diffused into the kesterite layer. As with lithium, the Na profiles seem to indicate that a large proportion of the alkali is trapped within the CdS buffer, being this more noticeable at higher PDA temperatures. Nevertheless, a sodium diffusion inside the kesterite film is clearly detected. Similar to Li, the results show an inhomogeneous Na distribution inside the absorber, with lower Na amount in the upper CZTS region (sputtering time \sim 1–20 s), higher concentration in the rear region (sputtering time \sim 20–35 s) and a final accumulation at the back interface (peak around 38–40 s). As discussed before, this profile is in accordance with the tendency of Na to segregate at interfaces and grain boundaries [34, 43–45], since a ‘double layer’ morphology is also observed in the Na-doped samples as it can be seen in SEM cross-sectional pictures

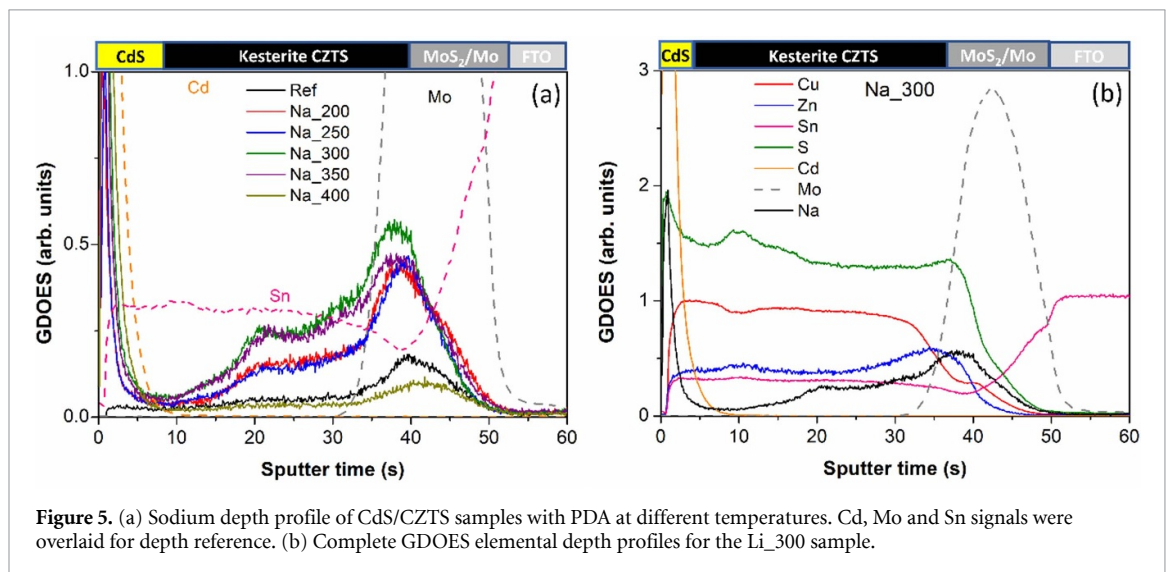
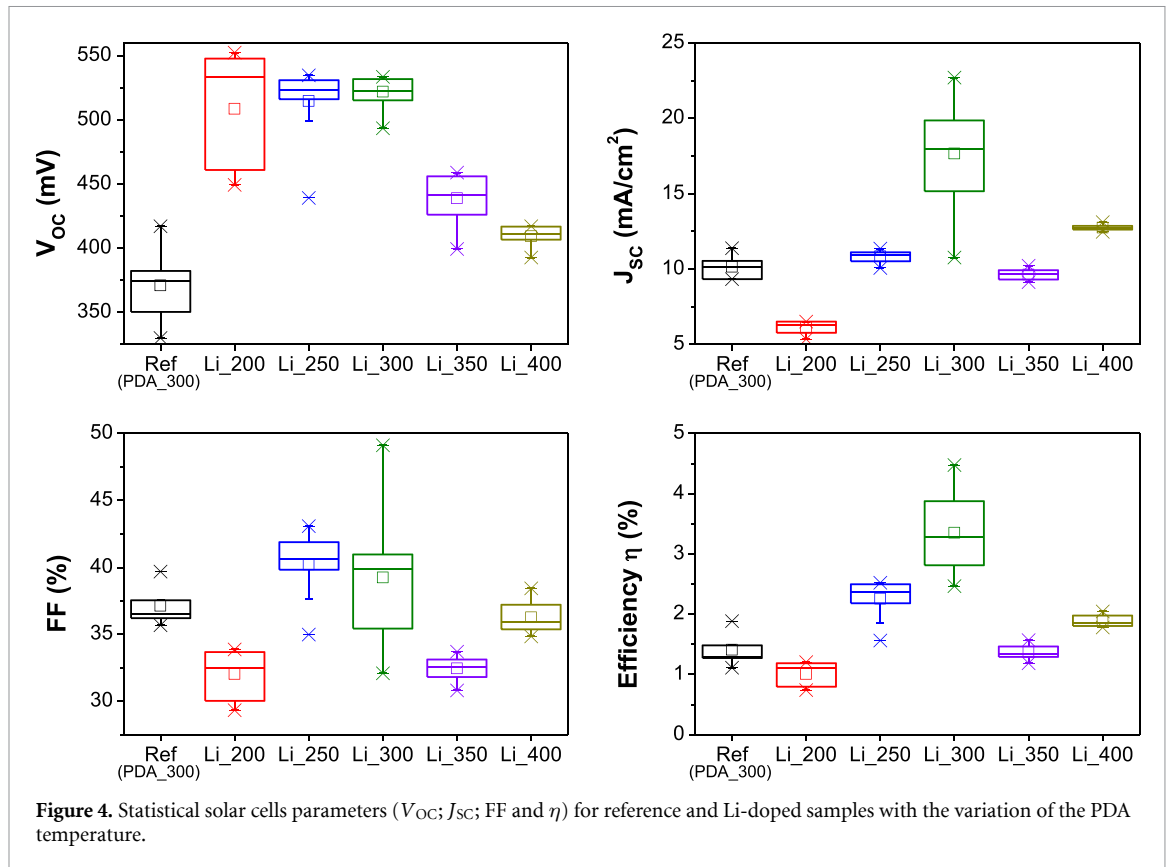


(figure 6). Unexpectedly, a small amount of accumulated sodium is detected at the back interface also in the reference sample. Based on previous results of our group, we expected the FTO acting as an efficient barrier for Na diffusion from the glass substrate. This might indicate that the FTO is not a perfect barrier, or it could be due to some type of contamination during processing [46]. Figure 5(b) shows a complete elemental depth profile of the Na-doped sample annealed at 300 °C. The kesterite element signals are arbitrarily scaled in order to reproduce the formula ratio. They show an, almost flat profile of Cu and Sn along the film thickness, whereas the zinc profile shows a peak close to the CZTS/Mo interface, likely revealing a ZnS segregation at the back side. A small Zn excess is also visible inside the CZTS film (sputtering time ~ 10 s), where Cu signal decreases while the S increases, matching the increase in Zn concentration. This result is difficult to explain and could suggest the presence of a Cu-poor region with segregation of secondary phases. Complete GDOES profiles for Na-doped samples are presented in the SI file (figure S2). PDA treatments have also been investigated to promote Cd diffusion through CdS/kesterite junction [6, 47]. At some extent, in this study we

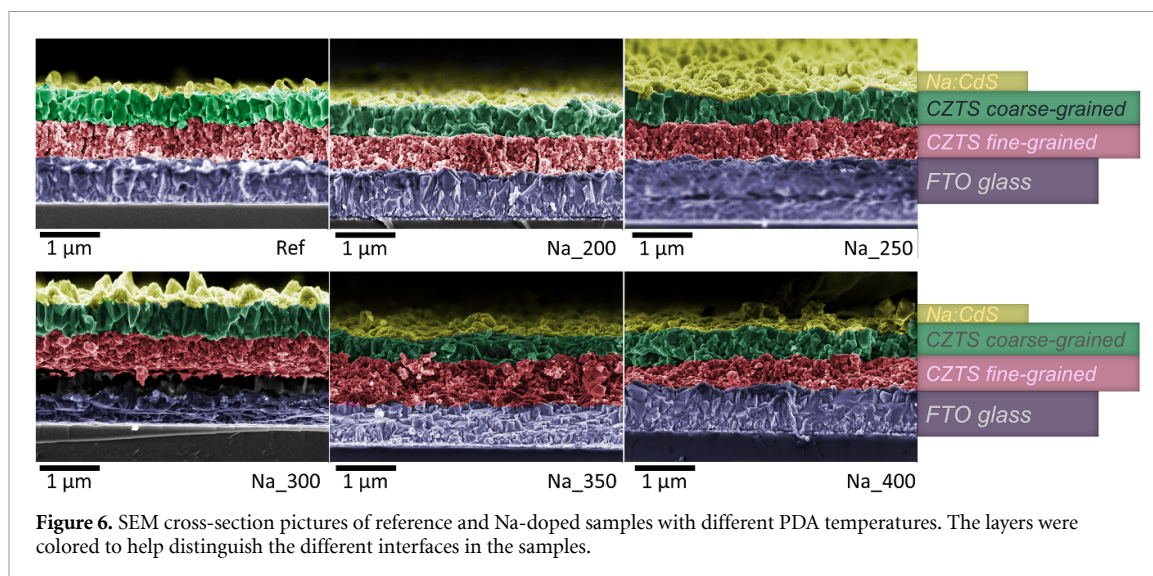


Figure 6. SEM cross-section pictures of reference and Na-doped samples with different PDA temperatures. The layers were colored to help distinguish the different interfaces in the samples.

initially aimed to promote alkali, and also, Cd diffusion. In the case of Na-doped samples, the GDOES measurements (figure S3, SI file) reveal a Cd signal only in the surface region of the samples, with only a slight broadening of the Cd profile as the PDA temperature increases. This result suggests that the effect of a possible cadmium diffusion is limited to the CdS/CZTS interface region, since Cd signal does not significantly extend into the bulk. Therefore, the differences in devices performance are not attributable to different Cd diffusions, but reasonably depend on the alkali doping. Figure 7 presents statistical optoelectronic parameters for the reference and Na doped samples with the effect of the PDA temperature. Interestingly, and in contrast with lithium doping, for sodium all PDA temperatures increase the efficiency of the devices comparing with the undoped reference, demonstrating the benefits of sodium incorporation into kesterite solar cells. As in the case of lithium, the addition of sodium markedly improves the open circuit of the cells and the FF of the devices improves over the reference only at intermediate PDA temperatures (250 °C–300 °C). On the other hand, the short-circuit current can be indicated as the parameter that still needs to be optimized. The low performance of this parameter can be related to the detrimental double-layer morphology and incomplete grain growth of the kesterite. Although in general the efficiency values are modest, they are above the average value of efficiencies reported for kesterite solar cells on transparent or semi-transparent substrates [26, 48–50]. It can be seen that Na-doping with an intermediate PDA temperature of 300 °C gathers the best PV parameters, reaching an efficiency of 3%. Both sodium and lithium provide an enhancement of the PV response. In particular, both alkalines substantially improve the V_{OC} of the devices with respect to the undoped sample. A more significant improvement in the short-circuit current (J_{SC}) was expected, knowing that the incorporation of these elements results in an improvement in the film morphology.

Table 2 summarizes the best PV parameters of the undoped and alkaline doped cells. Although the efficiencies are somewhat far from the record values, a noticeable effect of the incorporation of alkali can be observed. On average, the device doped with Na with PDA at 300 °C shows $\eta = 3\%$, compared to the reference (without Na) and treated at 300 °C as well, which yields an average efficiency of 2%. This implies an increase of 50% for the samples with sodium and more than 100% for the best device doped with lithium ($\eta = 4.5\%$). Despite this, the extent of the improvement is not always meaningful since it also depends on the quality of the starting reference device which need optimization. Another advantage of the proposed method compared to other PDT treatments is that it is not necessary to introduce a new process step to deposit the alkali source (like NaF or KF evaporation steps). The doping from the CBD solution could give also a better homogeneity if compared to other solution-based procedures, such as for instance the drop-casting approach, recently reported for CZTSSe devices [51].

Figure 8 presents the IQE of the devices under study. The IQE of the samples were calculated subtracting from the EQE of each device the transmittance and reflectance measured on the whole device according to the expression $IQE(\lambda) = EQE(\lambda)/(1 - (T(\lambda) + R(\lambda)))$. Interestingly, in the short wavelength region (350–500 nm), the IQE of alkali doped samples are significantly lower than the undoped reference device. This indicates a higher absorption of the doped-CdS buffer layer. Considering that the deposition time is the same, the growth kinetics of the CdS can be altered in the presence of a high concentration of alkali in the bath. However, a change in the optical properties due to the alkali doping of CdS is also not ruled out. In fact,

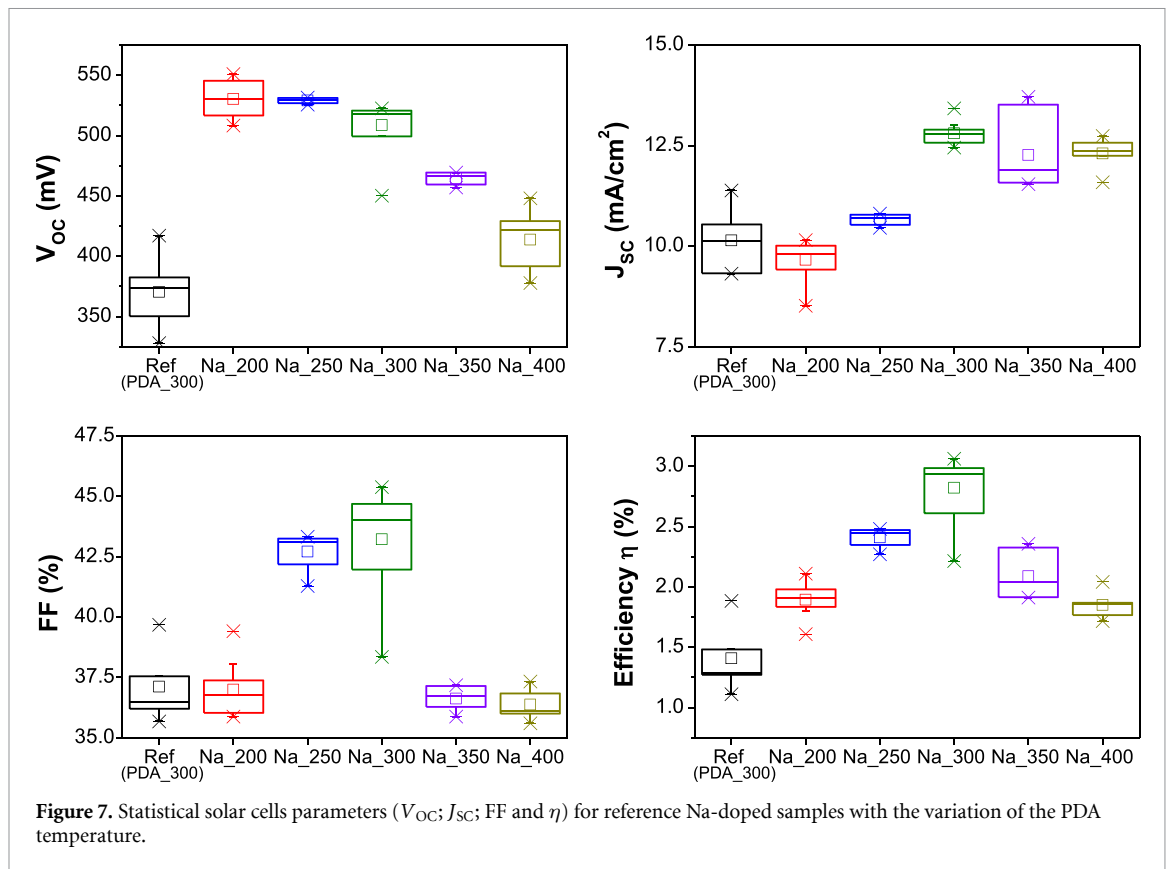


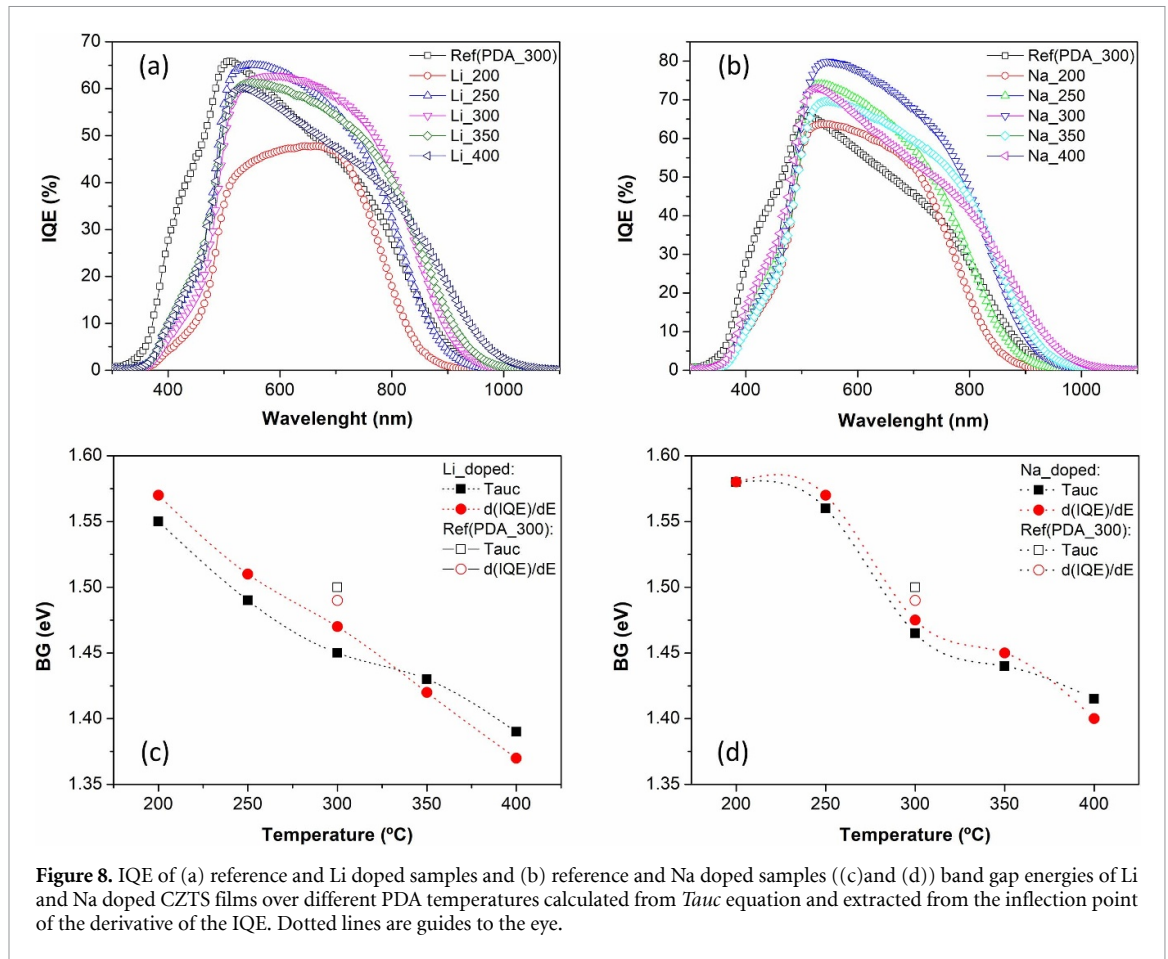
Table 2. Solar cells parameters of undoped and alkali doped CZTS devices.

Sample	J_{sc} (mA cm^{-2})	V_{oc} (mV)	FF (%)	η (%)
References (PDA_300)	11.4	417.1	39.7	1.9
<i>Li-doped devices</i>				
Li_200	6.5	547.7	33.9	1.2
Li_250	11.4	534.8	43.1	2.5
Li_300	22.7	533.7	49.1	4.5
Li_350	10.2	458.8	33.7	1.6
Li_400	13.1	416.8	38.4	2.1
<i>Na-doped devices</i>				
Na_200	10.2	550.8	39.4	2.1
Na_250	10.8	531.4	43.3	2.5
Na_300	13.4	522.6	45.4	3.1
Na_350	13.7	469.3	37.2	2.3
Na_400	12.7	448.0	36.8	2.0

Note: Bold values are intended to highlight improvement through the doping process.

according to the SIMS and GDOES depth profiles for Li and Na, respectively, we observed a significant amount of alkali inside the CdS layer. For the reference device, in the 500–800 nm range (related to the CZTS/CdS interface and CZTS absorbers properties) the IQE response falls sharply. On the contrary, alkali doped devices show an improved flatter response in that region, with the exception of the high temperature annealed device (400 °C) where the response falls quickly similar to the reference. Indeed, in the long wavelength range (800–1000 nm) the shape of the IQE response among the devices is not uniform and can be indicating a change in charge collection efficiency at long wavelengths [39]. The best spectral responses are obtained for the devices doped with lithium and sodium with PDA at intermediate temperatures (250 °C–300 °C for Li and 300 °C for Na) which in turn also deliver the best PV efficiencies and short circuit current densities.

To get a better understanding of the influence of the alkali doping on the PV response of these devices, figures 8(c) and (d) present the BG energies of the CZTS absorbers as a function of the PDA temperature.



A comparison of BG energies calculated using the *Tauc* plot for direct semiconductors [52], and the inflection point of the derivative of the IQE is also provided in the figures. (Complete set of figures can be seen in figure S7, SI file). The differences among values are within the expected deviation ranges using these methods as recently reported in [53, 54]. A clear influence of the PDA temperature on the BG value can be observed, independent of the Li/Na doping applied (see e.g. the reference devices). As the PDA temperature increases, the BG energy decreases, varying between 1.6–1.35 eV as the PDA temperature goes from 200 °C to 400 °C, as a consequence of the increase of the cation disordering level [16, 55, 56]. As expected, the PDA temperature increase causes a BG reduction of the kesterite and, as a consequence, a V_{OC} reduction of the corresponding PV devices, as observed in figures 4 and 7 for Li and Na doped samples respectively.

4. Conclusions

A novel and promising approach for alkali (Li and Na) doping of CZTS thin films has been implemented based on the introduction of alkali into the CBD process for CdS deposition, followed by a PDA treatment. The incorporation of both elements by this approach is effective as it is demonstrated using depth-profiling techniques (TOF-SIMS and GDOES). In particular, a significant amount of alkali stays inside the CdS layer, while parts of it diffuse into the kesterite. Another significant portion accumulates at the interface to the back contact (Mo/FTO), suggesting Li and Na segregations at grain boundaries. All devices doped with both lithium and sodium outperformed the PV response of the undoped reference sample. The PDA temperatures in the intermediate range (250–300) provided best alkali incorporation, allowing to improve the PV response of the devices by mainly increasing V_{OC} and FF of the cells. Best devices were obtained with a PDA at 300 °C leading to efficiencies of 4.5% and 3% for lithium and sodium, respectively. The limited PV response can be linked to the ‘double-layered’ kesterite morphology, which mainly reduces the J_{SC} and FF of the devices. Variations of the BG energy values are a consequence of the PDA treatment rather than alkali incorporation, and are attributed to a change in the order-disorder degree of cations in the kesterite sub-lattice, causing a V_{OC} reduction with the increase of the PDA temperature. Nonetheless, all the doped devices show higher V_{OC} compared to the reference cells, confirming the beneficial role of the alkali incorporation.

Data availability statement

The data that support the findings of this study are available upon reasonable request from the authors.











Acknowledgments

This work has received funding from the European Union's Horizon 2020 research and innovation program under Grant Agreement Nos. 777968 (INFINITE-CELL project). The authors gratefully acknowledge the help provided by the Spanish Ministry of Science, Innovation, and Universities under the IGNITE (ENE2017-87671-C3-1-R), by the European Regional Development Funds (ERDF, FEDER Programa Competitivitat de Catalunya 2007–2013), by the CERCA Programme/Generalitat de Catalunya. Authors from IREC belong to the SEMS (Solar Energy Materials and Systems) Consolidated Research Group of the 'Generalitat de Catalunya' (References 2017 SGR 862). A Hernandez thanks the Government of Spain for the FPI fellowship (BES-2015-074171). P Pistor thanks the European Union for his Marie Curie Individual Fellowship ('JUMPKEST', FP7-PEOPLE-2013-IEF-625840). ENEA researchers gratefully acknowledge the Italian Ministry of Economic Development for the support received in the framework of the Operating Agreement with ENEA for the Research on the Electric System. M Valdés acknowledges the financial support of the National Research Council (CONICET, Argentina, PIP 0175/16), Universidad Nacional de Mar del Plata (UNMdP, Argentina) and Agencia Nacional de Promoción Científica y Tecnológica (PICT 2425/18). The authors acknowledge to Nicolas Parducci in the edition of SEM images.

Conflict of interest

The authors declare that they have no known competing financial interests or personal relationships that could have appeared to influence the work reported in this paper.

ORCID iDs

M Valdés  <https://orcid.org/0000-0003-3104-3436>
A Hernández  <https://orcid.org/0000-0002-0895-3864>
Y Sánchez  <https://orcid.org/0000-0002-5740-1150>
R Fonoll  <https://orcid.org/0000-0002-6292-6648>
M Placidi  <https://orcid.org/0000-0001-5684-9669>
V Izquierdo  <https://orcid.org/0000-0002-5502-3133>
A Cabas-Vidani  <https://orcid.org/0000-0002-2692-5859>
M Valentini  <https://orcid.org/0000-0001-8567-7624>
A Mittiga  <https://orcid.org/0000-0001-8148-2707>
P Pistor  <https://orcid.org/0000-0002-9244-915X>
C Malerba  <https://orcid.org/0000-0001-6976-3442>
E Saucedo  <https://orcid.org/0000-0003-2123-6162>

References

- [1] Giraldo S, Jehl Z, Placidi M, Izquierdo-Roca V, Pérez-Rodríguez A and Saucedo E 2019 Progress and perspectives of thin film kesterite photovoltaic technology: a critical review *Adv. Mater.* **31** 1806692
- [2] Zakutayev A, Major J D, Hao X, Walsh A, Tang J, Todorov T K, Wong L H and Saucedo E 2021 Emerging inorganic solar cell efficiency tables (version 2) *J. Phys. Energy* **3** 032003
- [3] Lu S, Yang H, Li F, Wang Y, Chen S, Yang G, Liu Y and Zhang X 2018 Element substitution of kesterite $\text{Cu}_2\text{ZnSnS}_4$ for efficient counter electrode of dye-sensitized solar cells *Sci. Rep.* **8** 8714
- [4] Pal K, Singh P, Bhaduri A and Thapa K B 2019 Current challenges and future prospects for a highly efficient (>20%) kesterite CZTS solar cell: a review *Sol. Energy Mater. Sol. Cells* **196** 138–56
- [5] Green M, Dunlop E, Hohl-Ebinger J, Yoshita M, Kopidakis N and Hao X 2021 Solar cell efficiency tables (version 57) *Prog. Photovolt., Res. Appl.* **29** 3–15
- [6] Romanyuk Y E et al 2019 Doping and alloying of kesterites *J. Phys. Energy* **1** 044004
- [7] Haass S G, Diethelm M, Andres C, Romanyuk Y E and Tiwari A N 2017 Potassium post deposition treatment of solution-processed kesterite solar cells *Thin Solid Films* **633** 131–4
- [8] Kuo S Y and Hsieh M Y 2014 Efficiency enhancement in $\text{Cu}_2\text{ZnSnS}_4$ solar cells with subwavelength grating nanostructures *Nanoscale* **6** 7553–9
- [9] Xie H et al 2016 Impact of Na dynamics at the $\text{Cu}_2\text{ZnSn}(\text{S},\text{Se})_4/\text{CdS}$ Interface during post low temperature treatment of absorbers *ACS Appl. Mater. Interfaces* **8** 5017–24
- [10] Haass S G, Andres C, Figi R, Schreiner C, Bürki M, Romanyuk Y E and Tiwari A N 2018 Complex interplay between absorber composition and alkali doping in high-efficiency kesterite solar cells *Adv. Energy Mater.* **8** 1701760
- [11] Abzieher T, Schnabel T, Hetterich M, Powalla M and Ahlswede E 2016 Source and effects of sodium in solution-processed kesterite solar cells *Phys. Status Solidi a* **213** 1039–49

- [12] Haass S G, Diethelm M, Werner M, Bissig B, Romanyuk Y E and Tiwari A N 2015 11.2% efficient solution processed kesterite solar cell with a low voltage deficit *Adv. Energy Mater.* **5** 1500712
- [13] Werner M, Sutter-Fella C M, Romanyuk Y E and Tiwari A N 2015 8.3% efficient $\text{Cu}_2\text{ZnSn}(\text{S},\text{Se})_4$ solar cells processed from sodium-containing solution precursors in a closed reactor *Thin Solid Films* **582** 308–12
- [14] Rau U, Braunger D, Herberholz R, Schock H W, Guillemoles J F, Kronik L and Cahen D 1999 Oxygenation and air-annealing effects on the electronic properties of $\text{Cu}(\text{In},\text{Ga})\text{Se}_2$ films and devices *J. Appl. Phys.* **86** 497–505
- [15] Kobayashi T, Yamaguchi H and Nakada T 2014 Effects of combined heat and light soaking on device performance of $\text{Cu}(\text{In},\text{Ga})\text{Se}_2$ solar cells with $\text{ZnS}(\text{O},\text{OH})$ buffer layer *Prog. Photovolt., Res. Appl.* **22** 115–21
- [16] Malerba C, Valentini M and Mittiga A 2017 Cation disorder in $\text{Cu}_2\text{ZnSnS}_4$ thin films: effect on solar cell performances *Sol. RRL* **1** 1700101
- [17] Neuschitzer M et al 2015 Complex surface chemistry of kesterites: Cu/Zn reordering after low temperature postdeposition annealing and its role in high performance devices *Chem. Mater.* **27** 5279–87
- [18] Cui C, Kou D, Zhou W, Zhou Z, Yuan S, Qi Y, Zheng Z and Wu S 2022 Surface defect ordered $\text{Cu}_2\text{ZnSn}(\text{S},\text{Se})_4$ solar cells with efficiency over 12% via manipulating local substitution *J. Energy Chem.* **67** 555–62
- [19] Sanchez M F, Sanchez T G, Courel M, Reyes-Vallejo O, Sanchez Y, Saucedo E and Sebastian P J 2022 Effect of post annealing thermal heating on $\text{Cu}_2\text{ZnSnS}_4$ solar cells processed by sputtering technique *Sol. Energy* **237** 196–202
- [20] Sun K, Yan C, Huang J, Sun H, Jiang L, Deng X, Stride J, Hao X and Liu F 2018 Minority lifetime and efficiency improvement for CZTS solar cells via Cd ion soaking and post treatment *J. Alloys Compd.* **750** 328–32
- [21] Gershon T, Hamann C, Hopstaken M, Lee Y S, Shin B and Haight R 2015 Chemical consequences of alkali inhomogeneity in $\text{Cu}_2\text{ZnSnS}_4$ thin-film solar cells *Adv. Energy Mater.* **5** 1500922
- [22] Nakada T, Hirabayashi Y, Tokado T, Ohmori D and Mise T 2004 Novel device structure for $\text{Cu}(\text{In},\text{Ga})\text{Se}_2$ thin film solar cells using transparent conducting oxide back and front contacts *Sol. Energy* **77** 739–47
- [23] Valentini M, Malerba C, Serenelli L, Izzi M, Salza E, Tucci M and Mittiga A 2019 Fabrication of monolithic CZTS/Si tandem cells by development of the intermediate connection *Sol. Energy* **190** 414–9
- [24] Espindola-Rodriguez M, Sylla D, Sánchez Y, Oliva F, Grini S, Neuschitzer M, Vines L, Izquierdo-Roca V, Saucedo E and Placidi M 2017 Bifacial kesterite solar cells on FTO substrates *ACS Sustain. Chem. Eng.* **5** 11516–24
- [25] Ge J, Yu Y, Ke W, Li J, Tan X, Wang Z, Chu J and Yan Y 2016 Improved performance of electroplated CZTS thin-film solar cells with bifacial configuration *ChemSusChem* **9** 2149–58
- [26] Kim J-S, Kang J-K and Hwang D-K 2016 High efficiency bifacial $\text{Cu}_2\text{ZnSnSe}_4$ thin-film solar cells on transparent conducting oxide glass substrates *APL Mater.* **4** 096101
- [27] Sun J and Jasieniak J J 2017 Semi-transparent solar cells *J. Phys. D: Appl. Phys.* **50** 093001
- [28] Moon S H, Park S J, Hwang Y J, Lee D-K, Cho Y, Kim D-W and Min B K 2014 Printable, wide band-gap chalcopyrite thin films for power generating window applications *Sci. Rep.* **4** 4408
- [29] Xie H, Sánchez Y, López-Marino S, Espindola-Rodríguez M, Neuschitzer M, Sylla D, Fairbrother A, Izquierdo-Roca V, Pérez-Rodríguez A and Saucedo E 2014 Impact of $\text{Sn}(\text{S},\text{Se})$ secondary phases in $\text{Cu}_2\text{ZnSn}(\text{S},\text{Se})_4$ solar cells: a chemical route for their selective removal and absorber surface passivation *ACS Appl. Mater. Interfaces* **6** 12744–51
- [30] Sánchez Y, Giraldo S, Andrade-Arvizu J, Neuschitzer M, Calvo-Barrio L, Izquierdo-Roca V, Pérez-Rodríguez A and Saucedo E 2018 An innovative alkali doping strategy for $\text{Cu}_2\text{ZnSnSe}_4$ through the CdS buffer layer 2018 *IEEE 7th World Conf. on Photovoltaic Energy Conversion (WCPEC 2018)* pp 1645–7
- [31] Ur Rahman A, Sadiq T, Khan R, Anwar R, Gul B and Dahshan A 2022 Tunable electronic and magnetic properties of single layer CdS via Li substitutional doping: a first-principle study *J. Phys. Chem. Solids* **161** 110380
- [32] Samiyammal P, Parasuraman K and Balu A R 2019 Improved magnetic and photocatalytic properties of spray deposited (Li+Co) codoped CdS thin films *Superlattices Microstruct.* **129** 28–39
- [33] Cabas-Vidani A et al 2018 High-efficiency $(\text{Li}_x\text{Cu}_{1-x})_2\text{ZnSn}(\text{S},\text{Se})_4$ kesterite solar cells with lithium alloying *Adv. Energy Mater.* **8** 1801191
- [34] Andres C et al 2018 Decoupling of optoelectronic properties from morphological changes in sodium treated kesterite thin film solar cells *Sol. Energy* **175** 94–100
- [35] Schwarz T, Cojocaru-Miréidin O, Choi P, Mousel M, Redinger A, Siebentritt S and Raabe D 2015 Atom probe tomography study of internal interfaces in $\text{Cu}_2\text{ZnSnSe}_4$ thin-films *J. Appl. Phys.* **118** 095302
- [36] Li W, Chen J, Yan C and Hao X 2015 The effect of ZnS segregation on Zn-rich CZTS thin film solar cells *J. Alloys Compd.* **632** 178–84
- [37] Ge J, Chu J, Yan Y, Jiang J and Yang P 2015 Co-electroplated kesterite bifacial thin-film solar cells: a study of sulfurization temperature *ACS Appl. Mater. Interfaces* **7** 10414–28
- [38] Li J et al 2021 Large-grain spanning monolayer $\text{Cu}_2\text{ZnSnSe}_4$ thin-film solar cells grown from metal precursor *Small* **18** 2105044
- [39] Haass S G, Andres C, Figi R, Schreiner C, Bürki M, Tiwari A N and Romanyuk Y E 2018 Effects of potassium on kesterite solar cells: similarities, differences and synergies with sodium *AIP Adv.* **8** 015133
- [40] Khalil M I, Atici O, Lucotti A, Binetti S, Le Donne A and Magagnin L 2016 CZTS absorber layer for thin film solar cells from electrodeposited metallic stacked precursors ($\text{Zn}/\text{Cu}-\text{Sn}$) *Appl. Surf. Sci.* **379** 91–97
- [41] He J, Sun L, Chen Y, Jiang J, Yang P and Chu J 2015 Influence of sulfurization pressure on $\text{Cu}_2\text{ZnSnS}_4$ thin films and solar cells prepared by sulfurization of metallic precursors *J. Power Sources* **273** 600–7
- [42] Martinho F et al 2020 Persistent double-layer formation in kesterite solar cells: a critical review *ACS Appl. Mater. Interfaces* **12** 39405–24
- [43] Gershon T, Shin B, Bojarczuk N, Hopstaken M, Mitzi D B and Guha S 2015 The role of sodium as a surfactant and suppressor of non-radiative recombination at internal surfaces in $\text{Cu}_2\text{ZnSnS}_4$ *Adv. Energy Mater.* **5** 1400849
- [44] Jiang J et al 2020 Highly efficient copper-rich chalcopyrite solar cells from DMF molecular solution *Nano Energy* **69** 104438
- [45] Yuan Z-K, Chen S, Xie Y, Park J-S, Xiang H, Gong X-G and Wei S-H 2016 Na-diffusion enhanced p-type conductivity in $\text{Cu}(\text{In},\text{Ga})\text{Se}_2$: a new mechanism for efficient doping in semiconductors *Adv. Energy Mater.* **6** 1601191
- [46] Ould Salem M et al 2020 Over 10% efficient wide bandgap CIGSe solar cells on transparent substrate with Na predeposition treatment *Sol. RRL* **4** 2000284
- [47] Su Z et al 2020 Device postannealing enabling over 12% efficient solution-processed $\text{Cu}_2\text{ZnSnS}_4$ solar cells with Cd^{2+} substitution *Adv. Mater.* **32** 2000121
- [48] Mahajan S, Stathatos E, Huse N, Birajdar R, Kalarakis A and Sharma R 2018 Low cost nanostructure kesterite CZTS thin films for solar cells application *Mater. Lett.* **210** 92–96

- [49] Berruet M, Di Iorio Y, Pereyra C J, Marotti R E and Vázquez M 2017 Highly-efficient superstrate $\text{Cu}_2\text{ZnSnS}_4$ solar cell fabricated low-cost methods *Phys. Status Solidi* **11** 1700144
- [50] Leow S W, Li W, Tan J M R, Venkataraj S, Tunuguntla V, Zhang M, Magdassi S and Wong L H 2021 Solution-processed semitransparent CZTS thin-film solar cells via cation substitution and rapid thermal annealing *Sol. RRL* **5** 2100131
- [51] Punathil P, Artegiani E, Zanetti S, Lozzi L, Kumar V and Romeo A 2022 A simple method for Ge incorporation to enhance performance of low temperature and non-vacuum based CZTSSe solar cells *Sol. Energy* **236** 599–607
- [52] Tauc J 1970 Absorption edge and internal electric fields in amorphous semiconductors *Mater. Res. Bull.* **5** 721–9
- [53] Carron R *et al* 2019 Bandgap of thin film solar cell absorbers: a comparison of various determination methods *Thin Solid Films* **669** 482–6
- [54] Siebentritt S, Rey G, Finger A, Regesch D, Sendler J, Weiss T P and Bertram T 2016 What is the bandgap of kesterite? *Sol. Energy Mater. Sol. Cells* **158** 126–9
- [55] Valentini M, Malerba C, Menchini F, Tedeschi D, Polimeni A, Capizzi M and Mittiga A 2016 Effect of the order-disorder transition on the optical properties of $\text{Cu}_2\text{ZnSnS}_4$ *Appl. Phys. Lett.* **108** 211909
- [56] Scragg J J S, Choubrac L, Lafond A, Ericson T and Platzer-Björkman C 2014 A low-temperature order-disorder transition in $\text{Cu}_2\text{ZnSnS}_4$ thin films *Appl. Phys. Lett.* **104** 041911